SUPPLEMENTARY INFORMATION

SUPPLEMENTARY MATERIALS AND METHODS

Cell Line. A plasmid expressing GFP N-terminally linked to rat Pom121 (GFP-rPom121) was made by replacing the hNUP37 gene in a plasmid encoding EGFP-hNUP37 with the rPom121 gene from a plasmid encoding rPom121-3EGFP using HindIII and MfeI restriction sites. Plasmids expressing rPom121-3EGFP and EGFP-hNUP37 were gifts from J. Ellenberg (European Molecular Biology Laboratory, Heidelberg, Germany) (2). The EGFP-rPom121 coding sequence was confirmed by DNA sequencing. HeLa cells were transfected with the EGFP-rPom121 plasmid as described previously (4). Stable transformants were selected with Geneticin (0.4 g/500 mL, Invitrogen). A single colony was chosen and amplified to yield a stable cell line. Transfected HeLa cells were grown at 37°C, 5% CO_2 in Dulbecco's Modified Eagle Medium (D-MEM, GIBCO) containing 10% fetal bovine serum (GIBCO) and 0.4 g/L Geneticin.

Microscopy. Confocal and narrow-field epifluorescence images were obtained on the same inverted microscope setup (Zeiss Axiovert 200M) using a 1.46 NA 100X oil-immersion objective (Zeiss alpha Plan-Apochromat). Attached to the left side-port was a spinning-disk confocal unit (Yokagawa CSU-X1) equipped with an optical fiber for the excitation beam and a 512x512 EMCCD camera (Andor iXon DU-897) for image acquisition. On the right side-port was a 128x128 EMCCD camera (Roper Scientific Cascade 128) used for narrow-field epifluorescence imaging (5). A 2.5 W ArKr mixed-gas ion laser (Spectra-Physics) was used for 488 and 647 nm excitation. Green (GFP, NPCs) and dark red (Alexa647, cargo) narrow-field epifluorescence images were collected at 40 and 500 Hz, respectively, on the same EMCCD camera. A typical single molecule experiment was comprised of a series of green-dark red-green images all collected within 1 min to minimize error due to stage drift (0.2 ± 0.04 nm/s). The NPC images at the beginning and end of the image series were compared to ensure that sample movement did not occur during acquisition. Permeablized HeLa cells were prepared as described previously (5), and import experiments were performed in transport buffer [20 mM Hepes (pH 7.3), 110 mM KOAc, 5 mM NaOAc, 2 mM MgOAc, 1 mM EDTA, 1.5% polyvinylpyrrolidone (360 kDa, Sigma), and 2 mM dithiothreitol]. Photobleaching time for M9-βGal-8C was ~600 ms for most of the dyes (~80% reduction of initial emission intensity) and 800-1200 ms for complete photobleaching. Thus, photobleaching was essentially non-existent during imaging of NPC interaction times, which were < 10 ms.

Image Alignment. The image alignment error between fluorescence channels as determined with 0.1 um Tetraspeck microspheres (Invitrogen) was 4±3 nm (n = 24). The low error likely results from the small fields aligned, an objective (Zeiss 440782-9800-000 alpha Plan-Apochromat 100x/1.46) with lower aberrations than previously used (1, 4, 5), and the use of a multibandpass dichroic/emission filter combination (Semrock Di01-R405/488/561/635-25x36 and FF01-446/523/600/677-25), which obviated a filter change between fluorescence channels. Density maps were generated using the "Contour" function of OriginLab software.

Spatial Resolution. Static spatial precision was determined by repeated position measurements of single coverslip-adsorbed molecules. Due to

photobleaching, the static spatial precision of M9-βGal-8C was ~15 nm in the first ~80 ms of observation and ~17-19 nm in the first 200 ms. The diffusion constant of M9-βGal-8C labeled with eight Alexa647 molecules was 0.81±0.09 μm^2/s within the NPC (Figure S1), indicating that the average distance traveled during acquisition of 2 ms images was ~40 nm. Thus, the localization precision for moving M9-βGal-8C molecules was ~43-44 nm, estimated as described earlier (3).

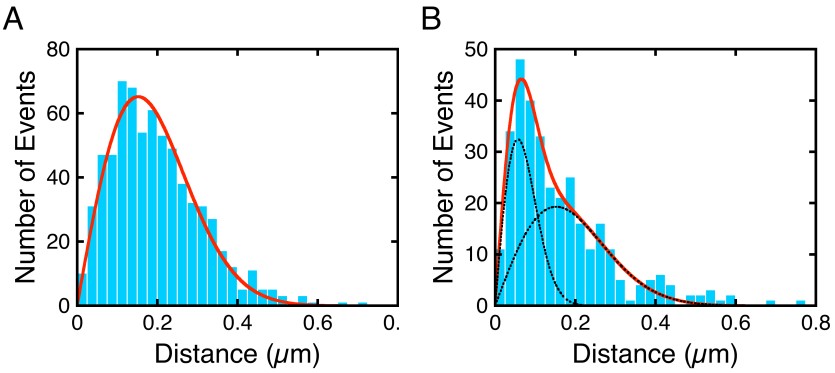

Figure S1. Single-molecule diffusion measurements. The diffusion constant of M9-βGal-8C labeled with eight Alexa647 molecules was obtained as described (1). (A) Frequency distribution of the distance traveled by an M9-βGal-8C molecule (saturated with transportin) in 2 ms within the cytoplasmic compartment of permeabilized cells (within ~5 μm of the NE). The data were fit to $p(\delta, \tau, D) = A^*p(\delta, \tau, D)$, yielding a diffusion constant D = 5.8±0.2 μm^2/s. (B) Frequency distribution of the distance traveled in 2 ms from the trajectories in Figure 3C. Data were fit to $p(\delta, \tau, D_0, D_2) = A^*p(\delta, \tau, D_0) + B^*p(\delta, \tau, D_2)$, yielding D_0 = 5.8±0.6 μm^2/s (61%) and D_2 = 0.81±0.09 μm^2/s (39%). Since D_0 is identical to the cytoplasmic diffusion constant obtained in (A), it is assumed that D_2 represents the diffusion constant of M9-βGal-8C when bound to the FG-network. [M9-βGal-8C] = 0.1 nM; [NTF2] = 1 μM; [RanGDP] = 0.5 μM; [GTP] = 1 mM; [transportin] = 1 μM.

The M9-β-Galactosidase Model Cargo. M9-βGal fully-labeled with 16 dye molecules translocated into nuclei in a signal-independent manner, indicating that large numbers of dye molecules can promote transport through the NPC. In addition, since β-Galactosidase is a disaccharide hydrolase (6), we were concerned that binding to and potential hydrolysis of polysaccharides within the NPC (7) would yield heterogeneous results and complicate interpretation. To address these issues, we reduced the number of dye labeling sites to 8 via two mutations (C76A and C1021S), and we reduced the βGal catalytic activity (k_{cat}) by ~10^5-fold and increased the K_M by ~50-fold with two mutations, E537Q and W999L (8, 9). We found that all four mutations were required to prevent signal-independent uptake of M9-βGal (Figure S2).

Transport Complexes. Gel filtration (Superose 6, Amersham-Pharmacia, optimal separation range 5-5000 kDa) was used to separate transport complexes from mixtures of transportin and M9-βGal-8C (unlabeled). When combined in ~25:1 ratio (transportin:cargo, T/C = 25), three major protein (A_{280}) peaks eluted between 11 mL and 16 mL (Figure S3A, black curve), which roughly correlate to molecular weights of ~1 MDa, ~500 kDa and ~100 kDa, respectively, based on the elution profile of protein standards (Gel Filtration Calibration Kits, GE Healthcare). The two lower molecular weight peaks are identified as M9-βGal-8C and transportin, respectively, based on the elution profiles of the pure proteins (Figure S3A, light blue (β) and orange (T) curves). The highest molecular weight peak (T4β) is consistent with M9-βGal-8C + 4 transportin molecules. Note that the largest protein standard used was thyroglobulin (670 kDa), and therefore, higher molecular weight peak assignments are approximate. To further support the T4β peak assignment, elution profiles of two additional mixtures were examined. For T/C = 1, the main peak

eluted at ~600 kDa, consistent with M9-βGal-8C + 1 transportin molecule (Figure S3B, dark blue curve, T1β). For T/C = 3, the main peak eluted at ~900 kDa, consistent with M9-βGal-8C + 3 transportin molecules (Figure S3B, green curve, T3β). No free transportin was found for these low T/C mixtures, consistent with a high binding affinity (K_D ≈ 42 nM (10)). These data indicate that the M9-βGal-8C is able to simultaneously bind 3-4 transportin molecules, and the transport complexes are stable enough to be resolved by size exclusion chromatography.

As an alternative approach to determine how many transportin molecules simultaneously bound to M9-βGal-8C, purified complexes were analyzed by stepwise photobleaching experiments (3). Transportin was modified at the C-terminus with a ybbR tag. This ybbR tag was covalently and specifically modified with a single CoA-Alexa647 dye molecule using Sfp phosphopantetheinyl transferase (11, 12). After enzymatic labeling of transportin-ybbR, the majority (>90%) of the unlinked CoA-Alexa647 was removed by one passage through a Zeba desalting column (2 mL, 7K MWCO, Thermo Scientific). The labeled transportin yields two fluorescent peaks upon Superose 6 gel chromatography (Figure S3C, red curve), consistent with

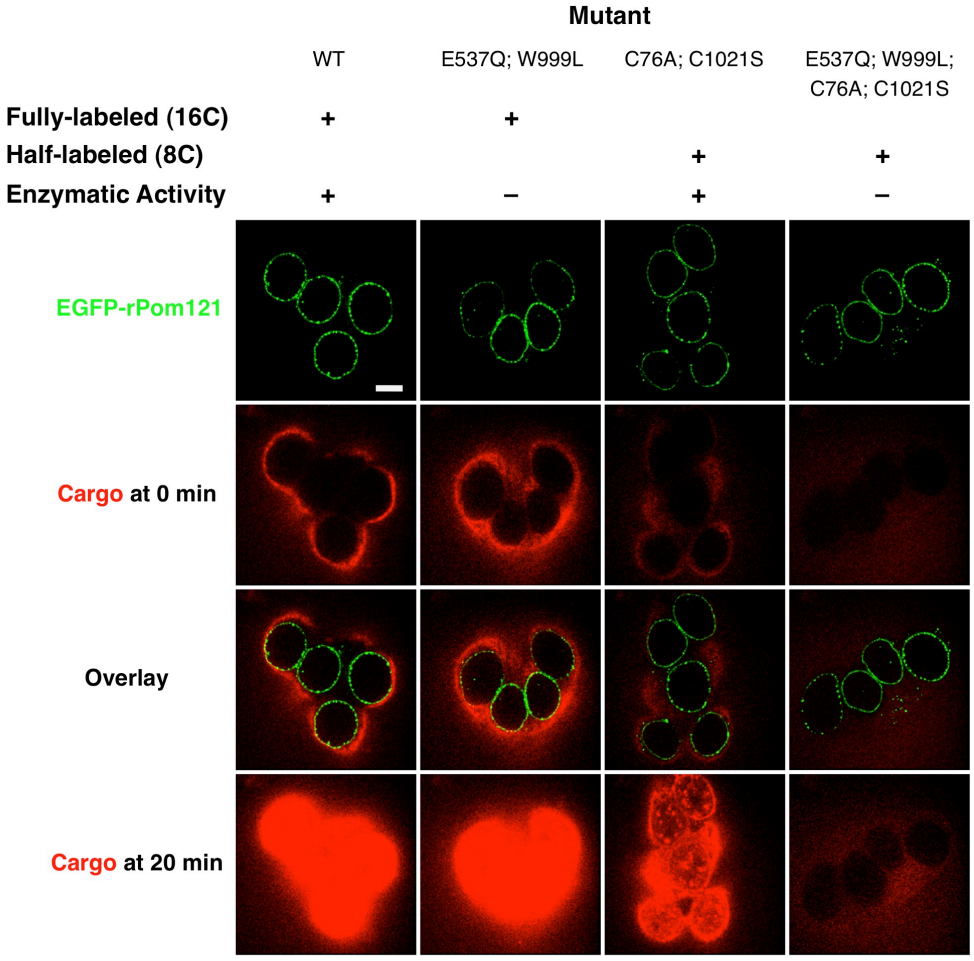

Figure S2. Effects of Decreasing the Number of Dye Labels and Reducing Sugar Binding and Hydrolase Activities on the Nuclear Transport of M9-βGal. Nuclear envelopes were visualized by EGFP-rPom121 fluorescence (*green*) and M9-βGal was visualized by Alexa647 fluorescence (*red*) using confocal microscopy. Fully-labeled wild-type M9-βGal (16C) binds to NPCs and enters the nucleoplasm of digitonin-permeabilized HeLa cells in the absence of transportin. Enzymatic mutations (E537Q and W999L) and cysteine mutations (C76A and C1021S), yielding M9-βGal-8C, are both required to prevent signal-independent nuclear uptake. See text for details. [M9-βGal] = 0.25 μM. Scale bar, 10 μm.

transportin-ybbR^{Alexa647} (T') and free (unreacted) CoA-Alexa647 (CoA). Three protein elution peaks were observed when M9-βGal-8C and transportin-ybbR^{Alexa647} were mixed (Figure S3C, violet curve, T/C = 8). The two lower molecular weight peaks are consistent with Sfp (~30 kDa) and free transportin-ybbR^{Alexa647} (~100 kDa). The major peak at ~1 MDa is consistent with M9-βGal-8C + 3-4 transportin molecules (T'3β-T'4β). The proteins in this peak were spread onto a microscope coverslip and imaged under stepwise photobleaching conditions (3) within 15 min after elution from the Superose 6 column (Figure S3D). Four distinct photobleach steps (and no more than 4) were observed for some fluorescent spots, supporting the hypothesis that M9-βGal-8C molecules can simultaneously bind up to four transportin molecules. The large number of spots that exhibited less than four photobleach steps is explained by incomplete dye labeling of transportin and/or complex decomposition after elution from the gel filtration column.

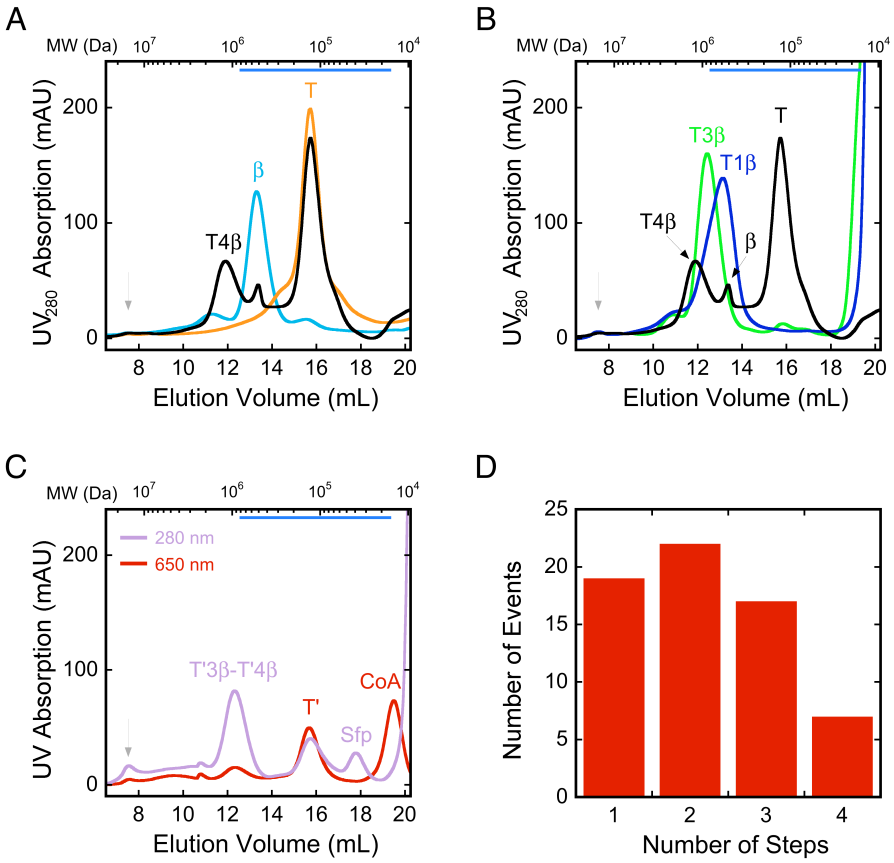

Figure S3. Size Exclusion Gel Chromatography and Stepwise Photobleaching of M9-βGal-8C NTR-Cargo Complexes. (A)-(C) Superose 6 gel filtration chromatography of transportin and the M9-βGal-8C cargo. Molecular weights based on 9 standard proteins (670 kDa to 13.7 kDa) are identified by the *y*-scale on the top, with the reliable region highlighted by the blue bar. The grey arrow indicates the void volume (> 5 MDa). Proteins were detected at 280 nm, unless otherwise indicated. The elution buffer was 50 mM Tris-HCl, 50 mM NaCl, 5 mM DTT (pH = 7.2). (A) Elution profile of a transportin:M9-βGal-8C mixture (T/C = 25, *black*). Elution profiles of M9-βGal-8C alone (*light blue*) and transportin alone (*orange*) are shown for comparison. (B) Elution profiles of T/C = 1 (*dark blue*) and 3 (*green*) transportin:M9-βGal-8C mixtures. The T/C = 25 elution profile from (A) is also shown (*black*) for comparison. (C) Elution profile of a transportin-ybbR^{Alexa647}:M9-βGal-8C mixture (T/C = 8, *violet*). The elution profile of transportin-ybbR^{Alexa647} monitored at 650 nm (detecting the Alexa647 dye) is shown for comparison (*red*). (D) Histogram of stepwise photobleaching events (3) observed for the T'3β-T'4β peak in (C) (*N* = 65). See text for details.

SUPPLEMENTARY DISCUSSION

EQUILIBRIUM THERMODYNAMICS OF MULTIVALENT BINDING

Multivalent Affinity (Avidity). Multivalency effects can be estimated as follows. This derivation is an extension of the approach followed by Yang et al (13). It is first assumed that each transportin molecule can interact with a single FG repeat. The result will then be expanded to multiple FG interactions per transportin molecule. For simplicity, it is assumed that the NTR-cargo complex of interest is the M9-βGal-8C cargo bound to four transportin molecules. If the NTR-cargo complex is in a homogeneous sea of FG repeats, the equilibria for the four sequential FG binding interactions are:

$$C + F \rightleftharpoons CF_1 \qquad K_{D1} = \frac{k_{off(D1)}}{k_{on(D1)}} = \frac{[C][F]}{[CF_1]} \tag{3}$$

$$CF_1 + F \rightleftharpoons CF_2 \qquad K_{D2} = \frac{k_{off(D2)}}{k_{on(D2)}} = \frac{[CF_1][F]}{[CF_2]} \tag{4}$$

$$CF_2 + F \rightleftharpoons CF_3 \qquad K_{D3} = \frac{k_{off(D3)}}{k_{on(D3)}} = \frac{[CF_2][F]}{[CF_3]} \tag{5}$$

$$CF_3 + F \rightleftharpoons CF_4 \qquad K_{D4} = \frac{k_{off(D4)}}{k_{on(D4)}} = \frac{[CF_3][F]}{[CF_4]} \tag{6}$$

where *C* and *F* represent the NTR-cargo complex and the FG repeats, respectively. Mass balance yields:

$$C_0 = [C] + [CF_1] + [CF_2] + [CF_3] + [CF_4] \tag{7}$$

where C_0 represents the initial concentration of the NTR-cargo complex. Solving in terms of [*C*] and [*F*] using Eqs. 3-6 yields:

$$C_0 = [C] + \frac{[C][F]}{K_{D1}} + \frac{[C][F]^2}{K_{D1}K_{D2}} + \frac{[C][F]^3}{K_{D1}K_{D2}K_{D3}} + \frac{[C][F]^4}{K_{D1}K_{D2}K_{D3}K_{D4}} \tag{8}$$

With a single transportin molecule in the NTR-cargo complex, the fraction of complexes bound to an FG repeat is given by:

$$\frac{[CF]}{C_0} = \frac{[F]}{K_{D1(1)} + [F]} \tag{9}$$

which is obtained by substituting $[C] = C_0 - [CF_1]$ into Eq. 3, and is a typical Langmuir binding isotherm. Here we include a parenthetical 1 in the K_{D1} term to indicate the binding affinity when there is only one transportin molecule in the NTR-cargo complex. As discussed below, the value of K_{D1} depends on the number of NTRs in the cargo complex. Analogously, the fraction of NTR-cargo complexes containing four transportin molecules that are bound to at least one FG repeat is:

$$\frac{[CF_1]+[CF_2]+[CF_3]+[CF_4]}{C_0}=\frac{C_0-[C]}{C_0}=\frac{[F]}{K_{app}+[F]} \tag{10}$$

or, using Eq. 8:

$$\frac{C_0-[C]}{C_0}=\frac{[F]}{\frac{K_{D1(4)}K_{D2}K_{D3}K_{D4}}{K_{D2}K_{D3}K_{D4}+K_{D3}K_{D4}[F]+K_{D4}[F]^2+[F]^3}+[F]} \tag{11}$$

where we have used $K_{D1(4)}$, which represents the initial binding affinity when there are four transportin molecules in the NTR-cargo complex. Formally, as described below, parenthetical numbers should be used for all the K_D's, but most are omitted for clarity. Eq. 11 is of the same form as Eq. 9, indicating that the apparent K_D, which describes the apparent affinity of an NTR-cargo complex with four transportin receptors for the FG-network, is:

$$K_{app}=\frac{K_{D1(4)}K_{D2}K_{D3}K_{D4}}{K_{D2}K_{D3}K_{D4}+K_{D3}K_{D4}[F]+K_{D4}[F]^2+[F]^3} \tag{12}$$

or:

$$\frac{K_{app}}{K_{D1(4)}}=\frac{1}{1+\frac{[F]}{K_{D2}}+\frac{[F]^2}{K_{D2}K_{D3}}+\frac{[F]^3}{K_{D2}K_{D3}K_{D4}}} \tag{13}$$

Note that K_{app} depends on each of the individual binding affinities and the FG concentration. Eq. 13 correspons to Eq. 1 in the main text.

Binding and Unbinding Rates. Differences in affinities implies differences in the local binding and unbinding rates of the NTR-cargo complexes from the FG-network. The equilibrium constants can be written in terms of kinetic rate constants as follows:

$$K_{D1(1)}=\frac{k_{off}}{k_{on}} \tag{14}$$

$$K_{D1(4)}=\frac{k_{off}}{4k_{on}} \tag{15}$$

where k_{off} and k_{on} are the intrinsic off- and on-times of a single FG repeat for a single binding site, and where, as mentioned earlier, the parenthetical numbers reflect the number of transportin molecules in the NTR-cargo complex. The on-rate for the NTR-cargo complex with four transportin molecules is four times higher due to the additional binding sites, which explains the differences in interaction frequencies at different transport:cargo ratios (Figure 2E). Similarly, the on-rates and off-rates for other binding and unbinding events is determined by the number of available FG binding sites:

$$\frac{1}{4}k_{on(D1)}=\frac{1}{3}k_{on(D2)}=\frac{1}{2}k_{on(D3)}=k_{on(D4)}=k_{on} \tag{16}$$

$$k_{off}=k_{off(D1)}=\frac{1}{2}k_{off(D2)}=\frac{1}{3}k_{off(D3)}=\frac{1}{4}k_{off(D4)} \tag{17}$$

The relationships between K_{D2}, K_{D3}, and K_{D4} can be estimated from Eqs. 16 and 17:

$$K_{D2} = \frac{4}{9} K_{D3} \tag{18}$$

$$K_{D2} = \frac{1}{6} K_{D4} \tag{19}$$

The apparent affinity, which includes the effect of multivalent interactions, can be written as:

$$K_{app} = \frac{k_{app}}{4k_{on}} \tag{20}$$

where k_{app} is the overall rate of release of all forms of the bound complexes to yield the FG-free complex. The ratio of off-times ($\tau = 1/k$) at high and low transportin concentrations can be estimated as:

$$\frac{\tau_{app}}{\tau_{off}} = \frac{k_{off}}{k_{app}} = \frac{K_{D1}}{K_{app}} \tag{21}$$

Thus, K_{app}/K_{D1} provides a measure of the effect of multivalency not only on the equilibrium binding affinity but also on the local unbinding times. If $K_{app}/K_{D1} < 1$, multivalent interactions lead to a higher binding affinity and a slower release rate. Combining Eqs. 13, 18, 19, and 22, the ratio of off-times in the presence and absence of multivalency is given by:

$$\frac{\tau_{app}}{\tau_{off}} = 1 + \left(\frac{[F]}{K_{D2}}\right) + \frac{4}{9}\left(\frac{[F]}{K_{D2}}\right)^2 + \frac{2}{27}\left(\frac{[F]}{K_{D2}}\right)^3 \tag{22}$$

which is equation (2) in the main text, and which agrees with Hlavacek et al. (14). Note that the local fluctuations in [*F*] due to the dissociation of FG-FG interactions as the FG-network undergoes structural rearrangements to accommodate the cargo complex has not been accounted for here. These effects are expected to be small relatively to the major enthalpic effects of multivalency that are described by the multiple *K*'s. The multivalency effects for multiple [*F*] and K_{D2} values are summarized in Figure 4.

Effect of Multiple FG Binding Sites on a Transportin Molecule. It is certainly possibly that transportin molecules contain more than one FG binding motif. Molecular dynamics simulations suggest that NTRs contain ≥ 6 sites that weakly interact with FG repeats (15-17), although only one primary and one secondary binding site were detected in crystallographic experiments on importin β1 (18). If one binding motif dominates over all others, multivalent effects should be largely predicted by the simple one binding site model (Eq. 22). On the other hand, if the multiple binding sites have similar affinities, the derivation is readily extended by increasing the number of binding equilibria. The general form of Eq. 22 is:

$$\frac{\tau_{app}}{\tau_{off}} = 1 + \sum_{i=1}^{4n-1} \left(\frac{2}{4n-1}\right)^i \left(\frac{(4n-1)(4n-2)...(4n-i)}{(i+1)!}\right)\left(\frac{[F]}{K_{D2}}\right)^i \tag{23}$$

where *n* is the number of FG binding sites on a transportin molecule. Following the lead for a similar derivation (14), Eq. 23 can also be written in terms of *K* (= k_{off}/k_{on}),

which is the intrinsic affinity of a single binding site on an NTR-cargo complex for an FG repeat:

$$\frac{\tau_{app}}{\tau_{off}} = 1 + \sum_{i=1}^{4n-1} \frac{(4n-1)(4n-2)...(4n-i)}{(i+1)!} \left(\frac{[F]}{K} \right)^i \qquad (24)$$

The effect of additional binding sites is illustrated in Figure S4. Comparison of Figure S4A with Figure 4 illustrates that the relationship between [*F*] and K_{D2} is much more important in determining τ_{app}/τ_{off} than the number of FG binding sites on the NTR. In contrast, the number of FG binding sites significantly modulates the effect of *K* on τ_{app}/τ_{off} (Figures S4B and S4C).

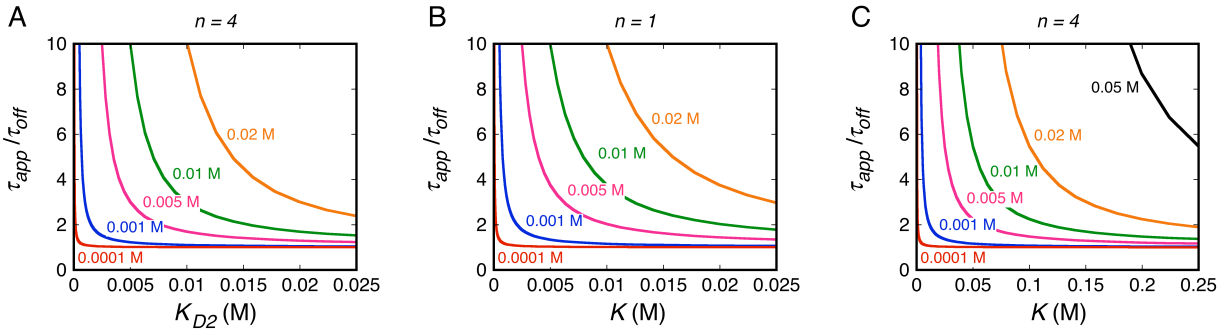

Figure S4. Effect of [*F*] on τ_{app}/τ_{off}. (A) τ_{app}/τ_{off} vs K_{D2} for n = 4 according to equation 23. Compare with Figure 4. (B & C) τ_{app}/τ_{off} vs K for n = 1 and n = 4, as indicated, according to equation 24. Note the different abscissa scale for C. The different [*F*] values for the various curves are identified in color.

Implications. While the lifetimes in Eqs. 22-24 describe the average time for the complex to release from the FG-network, they do not accurately reflect the time required to escape from the NPC (which is what is obtained from interaction time measurements in single molecule experiments) since the latter includes the time to diffuse through and out of the FG-network in the NPC, which could be significant. Nonetheless, Eqs. 22-24 indicate conditions under which multivalency is expected to be significant, namely, when [*F*] > K_{D2}. The data in Figure 2D reveal similar lifetimes for NTR-cargo complexes with 1-4 bound transportin molecules, indicating similar off-times, and thus, that multivalency effects are weak for the M9-βGal-8C cargo bound to four transportin molecules. This presents a serious conundrum since the total FG concentration in the central pore is normally estimated to be around 30 mM (19, 20) and NTR affinities for an FG repeat are typically estimated to be in the micromolar range or less (21-28). The solution may include some combination of the following: 1) the accessible or apparent FG concentration in the NPC is significantly lower than the total predicted FG concentration, e.g. due to FG-FG interactions, immobility, and/or a larger (less dense) FG cloud than anticipated; and 2) the FG affinity is strongly dependent on context, e.g., on the structural arrangement within the network and/or the energetic cost of disrupting the FG-network.

DIFFUSION IN AN EFFECTIVE POTENTIAL

Transport Efficiency. We assume that the movement of a cargo molecule through the NPC can be described as simple diffusion in an effective potential (Figure 6). There are several ways to calculate transport efficiency for this model that are more or less equivalent up to numerical prefactors that depend on the detailed assumptions of the dynamics near the pore entrance. The transport efficiency, i.e., the probability that a particle at y_1 reaches position y_5 (as opposed to y_0), is given by the following expression (29, 30):

$$P_{tr}(U) = \frac{\int_{y_0}^{y_1} \frac{e^{U(y)}}{D(y)} dy}{\int_{y_0}^{y_5} \frac{e^{U(y)}}{D(y)} dy} \tag{25}$$

where U is the potential energy and D is the diffusion constant of the particle. In the absence of RanGTP,

$$P_{tr}^{-Ran}(U) = \frac{1}{2 + 2\left[\frac{D_0 x_1}{D_1 x_0} e^{E_v} + \frac{D_0 x_2}{D_2 x_0} e^{E_b}\right]} \tag{26}$$

where D_0, D_1, and D_2 are the diffusion constants in the cytoplasm and the nucleoplasm, in the cytoplasmic and nucleoplasmic vestibules, and in the central permeability barrier, respectively. In the presence of RanGTP,

$$P_{tr}^{+Ran}(U) = \frac{1}{1 + e^{E_{Ran}} + \frac{D_0 x_1}{D_1 x_0}\left(\frac{3}{2} e^{E_v} + \frac{1}{2} e^{E_{Ran}}\right) + \frac{2 D_0 x_2}{D_2 x_0} e^{E_b}} \tag{27}$$

where we have assumed that RanGTP starts to act, on average, in the middle of the nucleoplasmic vestibule (Figure 6B). Assuming D_0 = 5.8 μm^2/s and D_2 = 0.8 μm^2/s (Figure S1), and that D_1 is approximately an average of D_0 and D_2 (i.e., 3.3 μm^2/s), P_{tr} is shown for various well depths and barrier heights in Figures 6 and S5 in both the absence and presence of RanGTP.

Interaction Time. An NTR-cargo complex's average interaction time with the NPC was described by Zilman et al (29). The mean interaction time, $\tau(U)$, depends both on the translocation time of cargos that pass through the pore and the time that cargos undergoing abortive transport spend at the pore, as described earlier (29-31). Here, we use the alternate expression:

$$\tau(U) = P_{tr}(U) \int_{y_0}^{y_5} \frac{e^{U(y)}}{D(y)} dy \int_{y_0}^{y} e^{-U(x)} dx - \int_{y_0}^{y_1} \frac{e^{U(y)}}{D(y)} dy \int_{y_0}^{y} e^{-U(x)} dx \tag{28}$$

where the limits refer to the model in Figure 6. Eq. 28 reduces to equation S(1) in the Zilman et al. paper after some term rearrangements. The mean interaction times in the absence and presence of RanGTP, respectively, are given by:

$$\tau(-Ran) = P_{tr}^{-Ran}\left[\begin{array}{l}\frac{2x_0}{D_0}\left(x_0 + x_1 e^{-E_v} + x_2 e^{-E_b}\right) \\ +\frac{2x_1}{D_1}\left(x_0 e^{E_v} + x_1 + x_2 e^{E_v - E_b}\right) \\ +\frac{2x_2}{D_2}\left(x_0 e^{E_b} + x_1 e^{E_b - E_v} + x_2\right)\end{array}\right] - \frac{x_0^2}{2D_0} \qquad (29)$$

$$\tau(+Ran) = P_{tr}^{+Ran}\left[\begin{array}{l}\frac{x_0}{D_0}\left[x_0\left(1+e^{E_{Ran}}\right) + x_1\left(\frac{1}{2}+\frac{3}{2}e^{E_{Ran}-E_v}\right) + 2x_2 e^{E_{Ran}-E_b}\right] \\ +\frac{x_1}{D_1}\left(x_0\left(\frac{3}{2}e^{E_v}+\frac{1}{2}e^{E_{Ran}}\right) + x_1\left(\frac{5}{4}+\frac{3}{4}e^{E_{Ran}-E_v}\right) + x_2\left(e^{E_v-E_b}+e^{E_{Ran}-E_b}\right)\right) \\ +\frac{2x_2}{D_2}\left(x_0 e^{E_b} + x_1 e^{E_b - E_v} + x_2\right)\end{array}\right] - \frac{x_0^2}{2D_0} \qquad (30)$$

Assuming the diffusion constants discussed earlier, τ is shown for various well depths and barrier heights in Figures 6 and S5 in both the absence and presence of RanGTP.

Axial Length of the FG-Nup "Cloud." In the discussion thus far, we have assumed that the axial length of the FG-Nup "cloud," the distance between the edges of the cytoplasmic and nucleplasmic vestibules furthest from the NPC center, is 200 nm, i.e., $2x_1 + 2x_2 = 200$ nm. We also examined the predicted effect of multivalency on transport efficiency and interaction times for $2x_1 + 2x_2 = 80$ nm (Figure S6). The central barrier width was again assumed to be 20 or 40 nm, but the vestibule widths were changed to 30 or 20 nm, respectively. These narrower vestibules may more accurately reflect the arrangement of the FG-Nup cloud within the NPC if all of the

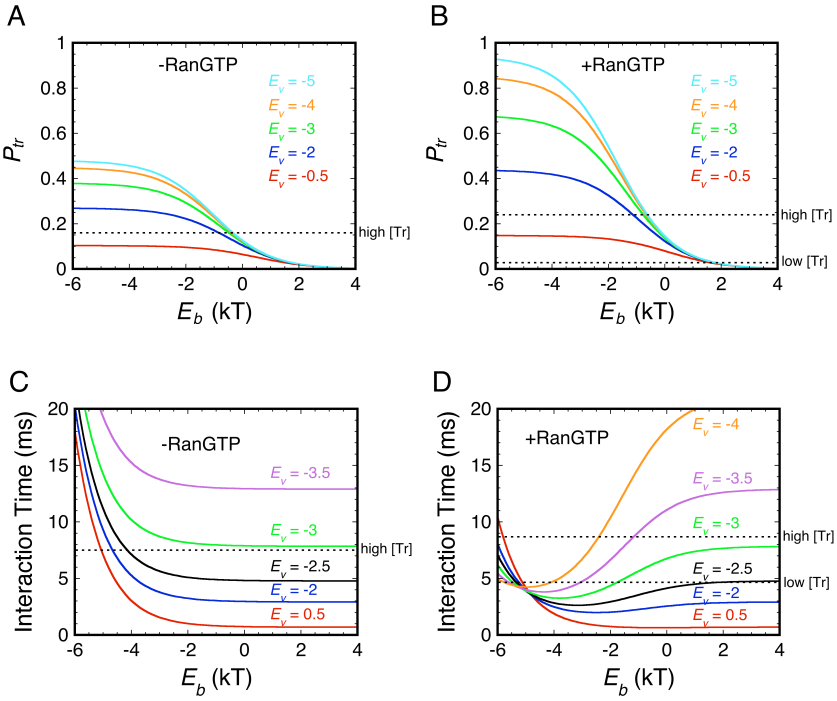

Figure S5. Transport efficiency (P_{tr}) and mean interaction time (τ) as a function of the barrier height (E_b) for various well depths (E_v), assuming a barrier width ($2x_2$), vestibule width (x_1), and escape distance (x_0) of 20, 90 and 25 nm, respectively. Comparison with Figure 6, in which a 40 nm barrier width was assumed, reveals only small differences. Experimentally determined values (Table S1) are indicated for low and high transportin (Tr) concentrations in the presence and absence of RanGTP by the horizontal dashed lines, as indicated.

FG-polypeptides are tethered to the core NPC scaffold and none are tethered to the cytoplasmic filaments or nuclear basket. Comparison with the data suggest barrier heights in the presence and absence of RanGTP similar to what was obtained earlier for the wider vestibules, but the vestibule depths are ~1-1.5 $k_B T$ deeper. The depths and widths of the vestibules primarily control interaction time, as this is where the cargo complexes spend most of the time, and transport probability is controlled primarily by the barrier height.

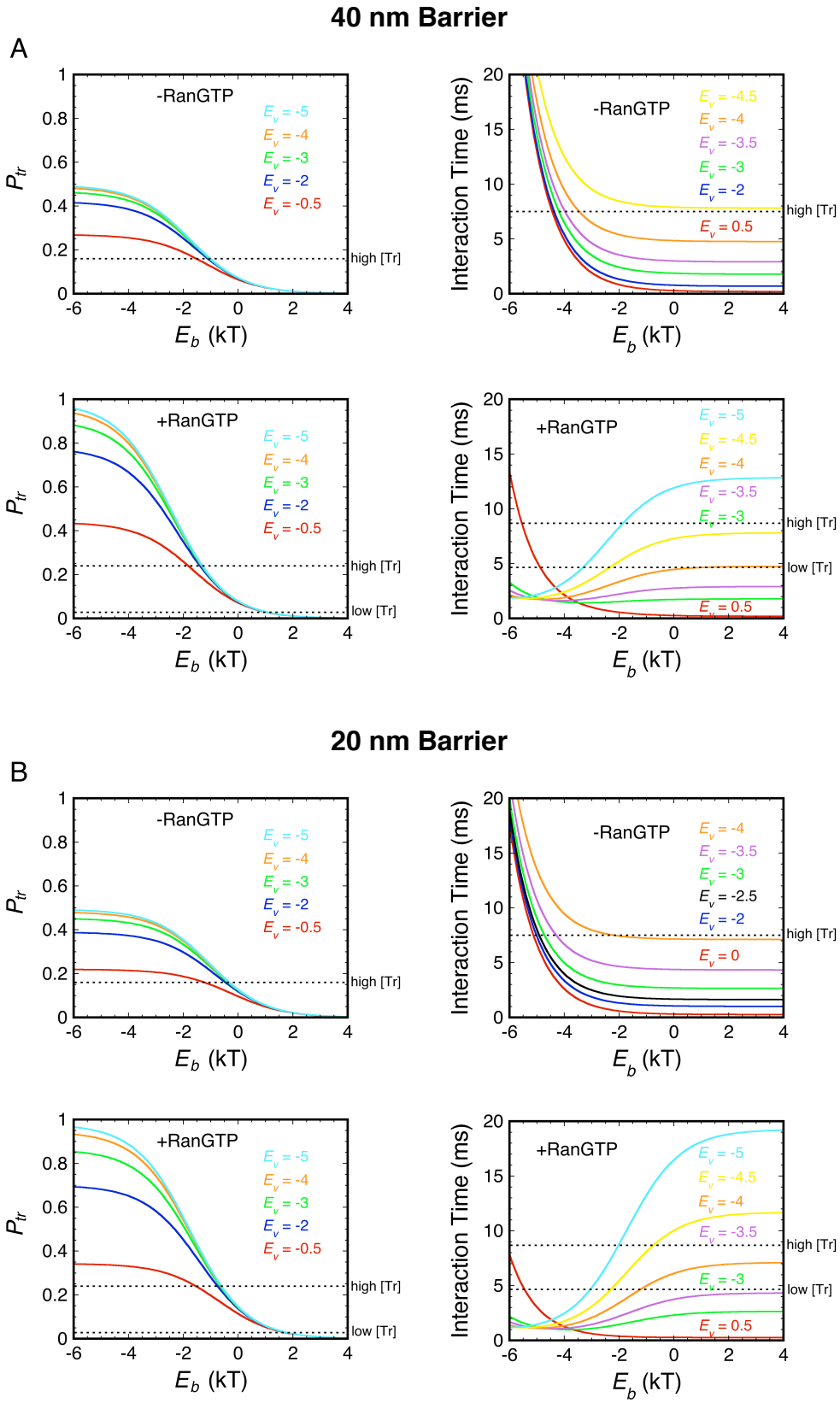

Figure S6. Transport efficiency (P_{tr}) and mean interaction time (τ) as a function of the barrier height (E_b) for various well depths (E_v), assuming an FG-Nup cloud of 80 nm. (A) The barrier width ($2x_2$), vestibule width (x_1) and escape distance (x_0) are 40, 20 and 25 nm, respectively. (B) The barrier width ($2x_2$), vestibule width (x_1) and escape distance (x_0) are 20, 30 and 25 nm, respectively. Experimentally determined values (Table S1) are indicated for low and high transportin (Tr) concentrations in the presence of absence and RanGTP by the horizontal dashed lines, as indicated. Comparison with Figures 6, S5 and S6, in which the FG-Nup cloud was 200 nm, reveals similar barrier heights under the various experimental conditions, but vestibule depths ~1-1.5 k_BT lower.

SUPPLEMENTARY REFERENCES

1. Yang W, Musser SM (2006) Nuclear import time and transport efficiency depend on importin β concentration. *J. Cell Biol.* 174:951-961.
2. Rabut G, Doye V, Ellenberg J (2004) Mapping the dynamic organization of the nuclear pore complex inside single living cells. *Nat. Cell Biol.* 6:1114-1121.
3. Yang W, Musser SM (2006) Visualizing single molecules transiting through nuclear pore complexes with narrow-field epifluorescence microscopy. *Methods* 39:3316-3328.
4. Sun C, Yang W, Tu L-C, Musser SM (2008) Single molecule measurements of importin α/cargo complex dissociation at the nuclear pore. *Proc. Natl. Acad. Sci. USA* 105:8613-8618.
5. Yang W, Gelles J, Musser SM (2004) Imaging of single-molecule translocation through nuclear pore complexes. *Proc. Natl. Acad. Sci. USA* 101:12887-12892.
6. Juers DH*, et al.* (2001) A structural view of the action of *Escherichia coli* (lacZ) beta-galactosidase. *Biochemistry* 40:14781-14794.
7. Panté N, Aebi U (1994) Towards the molecular details of the nuclear pore complex. *J. Struct. Biol.* 113:179-189.
8. Huber RE, Hakda S, Cheng C, Cupples CG, Edwards RA (2003) Trp-999 of beta-galactosidase (*Escherichia coli*) is a key residue for binding, catalysis, and synthesis of allolactose, the natural lac operon inducer. *Biochemistry* 42:1796-1803.
9. Yuan J, Martinez-Bilbao M, Huber RE (1994) Substitutions for Glu-537 of beta-galactosidase from *Escherichia coli* cause large decreases in catalytic activity. *Biochem. J.* 299:527-531.
10. Lee BJ*, et al.* (2006) Rules for nuclear localization sequence recognition by karyopherin β2. *Cell* 126:543-558.
11. Yin J, Lin AJ, Golan DE, Walsh CT (2006) Site-specific protein labeling by Sfp phosphopanthetheinyl transferase. *Nat. Protocols* 1:280-285.
12. Yin J*, et al.* (2005) Genetically encoded short peptide tag for versatile protein labeling by Sfp phosphopantetheinyl transferase. *Proc. Natl. Acad. Sci. USA* 102:15815-15820.
13. Yang T, Baryshnikova OK, Mao H, Holden MA, Cremer PS (2003) Investigations of bivalent antibody binding on fluid-supported phospholipid membranes: the effect of hapten density. *J. Am. Chem. Soc.* 125:4779-4784.
14. Hlavacek WS, Percus JK, Percus OE, Perelson AS, Wofsy C (2002) Retention of antigen on follicular dentritic cells and B lymphocytes through complement-mediated multivalent ligant-receptor interactions: theory and application to HIV treatment. *Math. Biosci.* 176:185-202.

15. Isgro TA, Schulten K (2005) Binding dynamics of isolated nucleoporin repeat regions to importin-beta. *Structure* 13(12):1869-1879.
16. Isgro TA, Schulten K (2007) Association of nuclear pore FG-repeat domains to NTF2 import and export complexes. *J. Mol. Biol.* 266:330-345.
17. Isgro TA, Schulten K (2007) Cse1p-binding dynamics reveal a binding pattern for FG-repeat nucleoporins on transport receptors. *Structure* 15(8):977-991.
18. Bayliss R, Littlewood T, Stewart M (2000) Structural basis for the interaction between FxFG nucleoporin repeats and importin β in nuclear trafficking. *Cell* 102:99-108.
19. Peleg O, Lim RY (2010) Converging on the function of intrinsically disordered nucleoporins in the nuclear pore complex. *Biol. Chem.* 391(7):719-730.
20. Stewart M (2007) Molecular mechanism of the nuclear protein import cycle. *Nat. Rev. Mol. Cell Biol.* 8:195-208.
21. Ben-Efraim I, Gerace L (2001) Gradient of increasing affinity of importin β for nucleoporins along the pathway of nuclear import. *J. Cell Biol.* 152:411-417.
22. Gilchrist D, Mykytka B, Rexach M (2002) Accelerating the rate of disassembly of karyopherin•cargo complexes. *J. Biol. Chem.* 277:18161-18172.
23. Pyhtila B, Rexach M (2003) A gradient of affinity for the karyopherin Kap95p along the yeast nuclear pore complex. *J. Biol. Chem.* 278:42699-42709.
24. Lott K, Bhardwaj A, Mitrousis G, Pante N, Cingolani G (2012) The importin β binding domain modulates the avidity of importin β for the nuclear pore complex. *J. Biol. Chem.* 285:13769-13780.
25. Bayliss R, Littlewood T, Strawn LA, Wente SR, Stewart M (2002) GLFG and FxFG nucleoporins bind to overlapping sites on importin-β. *J. Biol. Chem.* 277:50597-50606.
26. Bayliss R*, et al.* (1999) Interaction between NTF2 and xFxFG-containing nucleoporins is required to mediate nuclear import of RanGDP. *J. Mol. Biol.* 293:579-593.
27. Tetenbaum-Novatt J, Hough LE, Mironska R, McKinney SA, Rout MP (2012) Nucleocytoplasmic transport: a role for nonspecific competition in karyopherin-nucleoporin interactions. *Mol. Cell. Proteomics* 11:31-46.
28. Ribbeck K, Görlich D (2001) Kinetic analysis of translocation through nuclear pore complexes. *EMBO J.* 20:1320-1330.
29. Zilman A, Di Talia S, Chait BT, Rout MP, Magnasco MO (2007) Efficiency, selectivity, and robustness of nucleocytoplasmic transport. *PLoS Comp. Biol.* 3:1281-1290.
30. Gardiner CW (2004) *Handbook of Stochastic Methods for Physics, Chemistry and the Natural Sciences* (Springer-Verlag).

31. Berezhkovskii AM, Pustovoit MA, Bezrukov SM (2003) Channel-facilitated membrane transport: average lifetimes in the channel. *J. Chem. Phys.* 119:3943.

Table S1: Single Molecule Statistics for Nuclear Import of M9-βGal-8C at Different Transportin Concentrations[1]

Transportin to M9-βGal-8C Ratio	RanGTP[2]	Interaction Time (ms)	*N*[3]	Import Efficiency (%)	*N*[4]	NE Interaction Frequency (events μm^{-1} s^{-1})	*N*[5]	Cargo Oligomerization State[6] $C:CT_1:CT_2:CT_3:CT_4$ (% of total)	$CT_2 + CT_3 + CT_4$ (% of total)
0:1	+					0.08 ± 0.03	4		
1:4	+	4.8 ± 0.4	198	3 ± 2	59	0.8 ± 0.1	4	78 : 20 : 2.0 : 0.09 : < 0.01	2.1 %
1:4	-					0.2 ± 0.1	3		
1:4 (pre-washed with RanGTP)[7]	+					0.6 ± 0.2	3		
1:4 (pre-washed with RanGTP)[7]	-					0.1 ± 0.1	3		
1:1	+	6.1 ± 0.5	212	13 ± 3	103	1.3 ± 0.2	3	32 : 42 : 21 : 4.5 : 0.36	26 %
4:1	+	7.5 ± 0.6	200	21 ± 3	151	2.0 ± 0.3	3	0.04 : 0.97 : 8.9 : 36 : 54	99 %
5,000:1	+	7.3 ± 1.2	77	21 ± 3	136	2.3 ± 0.2	3	< 0.01 : 0.17 : 3.1 : 24 : 72	99%
10,000:1	+	8.7 ± 0.8	198	24 ± 4	135	2.2 ± 0.1	3	< 0.01 : 0.03 : 0.90 : 14 : 85	100%
10,000:1	-	7.5 ± 0.6	238	16 ± 3	129	2.3 ± 0.4	4		
10,000:1 (pre-washed with transportin)[8]	-	5.6 ± 0.5	185	15 ± 5	62	0.8 ± 0.3	3		

[1]Unless otherwise noted, concentrations during single molecule import experiments were: [M9-βGal-8C] = ~0.1 nM, [NTF2] = 1 μM.

[2]When present, the RanGTP concentration was 0.5 μM (shorthand notation for 0.5 μM RanGDP + 1 mM GTP).

[3]*N* (number of events) for the interaction time.

[4]*N* (number of events) for the import efficiency.

[5]*N* (number of cells) for the interaction frequency.

[6]Theoretical cargo oligomerization states were calculated based on a binomial distribution using an M9-transportin dissociation constant of 42 nM (10) to estimate binding probability. For the two highest transportin:cargo ratios, the cargo was simply diluted into transport buffer containing 0.5 or 1 μM transportin, and incubated for ≥ 20 min on ice before adding to permeablized cells. For the three lowest ratios, transportin and cargo were first mixed at a higher concentration (0.2-2 μM transportin) to speed binding and mitigate loss by adsorption to the vessel walls. After a ≥ 20 min incubation on ice, the solution was diluted to a final cargo concentration of ~0.1 nM, and experiments were completed within 3 min after dilution. The oligomerization state distribution was calculated for the higher concentration, and therefore conservatively estimates the number of M9-transportin interactions (highest possible number of interactions, disregarding potential dissociation upon dilution).

[7]Permeabilized cells were preincubated with 0.5 μM RanGTP for 10 min.

[8]Permeabilized cells were preincubated with 0.5 μM transportin for 10 min. Pre-incubation of nuclei with transportin to dissociate endogenous RanGTP from NPCs resulted in a shorter interaction time and decreased interaction frequency, but did not affect the import efficiency. These data indicate that some import events are RanGTP independent. Under these conditions, excess transportin that binds to NPCs dissociates slowly (not shown), suggesting that RanGTP is not required for transportin to dissociate from NPCs, and that transportin accumulates at NPCs in the absence of RanGTP. The decreased interaction frequency can be explained by NPC-bound transportin interfering with the binding of incoming cargo complexes.

Videos

For both videos, the pixel size is ~240 nm, each frame was acquired in 2 ms, and playback speed is 5 frames per second.

Video 1) Movie of the abortive event shown in Fig. 1C (top). (*green*) GFP (EGFP-rPom121) fluorescence intensity; (*red*) cargo (M9-βGal-8C-Alexa647) fluorescence intensity.

Video 2) Movie of the entry event shown in Fig. 1C (bottom). (*green*) GFP (EGFP-rPom121) fluorescence intensity; (*red*) cargo (M9-βGal-8C-Alexa647) fluorescence intensity.